Computational study of Li_3BO_3 and Li_3BN_2 II: Stability analysis of pure phases and of model interfaces with Li anodes

Yan Li [1], Zachary D. Hood [2], and N. A. W. Holzwarth [1]

[1]*Department of Physics, Wake Forest University, Winston-Salem, North Carolina 27109, USA*
[2]*Applied Materials Division, Argonne National Laboratory, Argonne, Illinois 60439, USA*

Both Li_3BO_3 and Li_3BN_2 materials have promising properties for use in all solid-state batteries and other technologies dependent on electrolytes with significant ionic conductivity. As the second of a two-part study, the structural properties of Li_3BO_3 and three reported phases of Li_3BN_2 are investigated using first-principles modeling techniques. For α-Li_3BN_2, the tetragonal $P4_2/mnm$ structure reported in the literature is found to be unstable as evidenced by imaginary phonon modes near the M point of its Brillouin zone. Our simulations within the harmonic approximation suggest that the real α phase has the orthorhombic space group symmetry $Pmmn$ formed with twice as many formula units and tiny adjustments of the equivalent lattice parameters and fractional coordinates. Extending the analysis of the $Pmmn$ α-Li_3BN_2 structure to the quasiharmonic approximation improves the agreement between the room-temperature x-ray pattern reported in the literature and the corresponding simulation results. In anticipation of the use of the monoclinic phases of Li_3BO_3 and Li_3BN_2 in Li ion conducting applications, chemical stability is investigated in terms of free-energy differences of possible decomposition and Li reaction processes, finding encouraging results. As further investigations of Li_3BO_3 and β-Li_3BN_2 as electrolyte or coating materials, particularly for use with Li metal anodes, idealized electrolyte/Li interfaces were investigated in terms of their geometric, energetic, and electronic properties. The results find the electrolyte/Li interfaces to be quite favorable, perhaps comparable to the pioneering LiPON/Li system.

I. INTRODUCTION

The companion paper (Paper I) [1] presents the results of first-principles computational methods used to investigate the detailed mechanisms of Li ion diffusion in the monoclinic forms of lithium borate Li_3BO_3 and boron-nitride Li_3BN_2, finding encouraging results for ionic conductivity with the introduction of vacancies by disorder and doping. In the present paper, we examine the stability properties of pure Li_3BO_3 and Li_3BN_2, including the stability of the crystalline materials and the stability of possible interface configurations with an ideal lithium anode in anticipation of possible applications as electrolytes or as coatings in solid-state batteries and other technologies.

The outline of this paper is as follows. Section II details the computational methods used in this paper. Section III presents the structural properties of Li_3BO_3 and three reported phases of Li_3BN_2, including the calculated lattice parameters of the crystal structures and vibrational analyses using the harmonic phonon approach. To improve the physical treatment, in Sec. IV, the quasiharmonic approximation is applied to better represent the corrected structure of α-Li_3BN_2. Section V discusses the stabilities of the materials in terms of possible decompositions and reactions with Li metal. In Sec. VI, we investigated the interface properties of the potential electrolyte materials, Li_3BO_3 and β-Li_3BN_2, with Li metal. A summary of the results and some conclusions are given in Sec. VII.

II. CALCULATIONAL METHODS

The computational methods for this paper are based on density functional theory (DFT) [2,3] using the projector augmented plane wave (PAW) [4] formalism with the data sets generated by the ATOMPAW code [5]. The exchange-correlation terms were represented by the modified generalized gradient formulation known as PBEsol [6]. Density functional perturbation theory [7–11] was used to evaluate derivatives of the density functional energies. The computations were performed using both the ABINIT [12,13] and QUANTUM ESPRESSO [14,15] packages interchangeably. For reasons of convenience and efficiency, ABINIT was used to perform the calculations reported in Secs. III and V while QUANTUM ESPRESSO was used to perform the calculations reported in Secs. IV and VI. The two codes use slightly different internal algorithms to evaluate the system energies, so it was necessary to use slightly different calculational parameters. For example, for each Bloch wave vector $\mathbf{k}$, the summations over reciprocal lattice vectors $\mathbf{G}$ included all terms such that $|\mathbf{k} + \mathbf{G}|^2 \leqslant 2m\epsilon_{cut}/\hbar^2$ (where m denotes the electron mass). By choosing ϵ_{cut} to be 50 and 81 Ry for ABINIT and QUANTUM ESPRESSO, respectively, equivalent results were obtained. On the other hand, other parameters such as the Brillouin zone sampling worked equally well in the two codes. For static lattice calculations, performed in the conventional cells, Brillouin-zone sampling grids [16]

were set to $12 \times 4 \times 4$ for Li_3BO_3 and $12 \times 12 \times 12$, $6 \times 6 \times 8$, $12 \times 12 \times 12$, and $6 \times 6 \times 8$ for Li_3BN_2 in the $P2_1/c$, $I4_1/amd$, $P4_2/mnm$, and $Pmmn$ structures, respectively. For interface calculations described in Sec. VI, larger supercells were constructed and the Brillouin zone sampling was adjusted accordingly.

The phonon calculations were performed in the primitive unit cells, following the approach described in previous work [17] using phonon wave-vector grids sufficient to represent the dynamical matrices at high symmetry **q** points to obtain accurate phonon densities of states using interpolation methods. The **q**-point grids were chosen to be $6 \times 2 \times 2$ for Li_3BO_3, and $4 \times 4 \times 4$, $3 \times 3 \times 3$, $4 \times 4 \times 4$, and $3 \times 3 \times 4$ for the four considered structures of Li_3BN_2.

In Sec. IV MATLAB [18] and Python [19] were used to aid the calculations, particularly for evaluating interpolation algorithms.

Visualizations of the structural configurations were obtained using the VESTA [20] and XCRYSDEN [21] programs. The software FINDSYM [22] helped in space-group analysis of the optimized structures. The MERCURY software package [23] was used to analyze x-ray patterns.

III. STRUCTURAL STABILITY IN THE HARMONIC APPROXIMATION

To evaluate the dynamical stability of the materials under consideration, we adopted the methodologies used in previous work [17] based on DFT [2,3] to represent the electronic ground state and the Born-Oppenheimer approximation [24] and the harmonic phonon approximation [7,25] to estimate the vibrational contribution to the Helmholtz free energy. The detailed equations are presented in Ref. [17], but some of the equations are given as follows. Self-consistent DFT performed on a unit cell of the material, optimizing the lattice parameters and internal coordinates, provides an excellent representation of the equilibrium static lattice internal energy U_{SL} of the system. Comparing the computed optimized lattice parameters and internal coordinates with experimentally measured values offers a quantitative estimate of the validity of the calculation and the measurement.

Since the materials of interest are electronically insulating, there are no temperature-dependent electronic contributions, so the equilibrium static lattice free energy is also temperature independent and well-approximated by U_{SL}. To estimate the contributions to the Helmholtz free energy due to temperature-dependent lattice vibrations, density-functional perturbation theory [8,9,26] is used to evaluate second-order derivatives of U_{SL} with respect to atomic displacements as is necessary to compute the dynamical matrix and the normal mode frequencies $\omega^\nu(\mathbf{q})$ as a function of wave vector **q**. The dependence of $\omega^\nu(\mathbf{q})$ on wave vector **q** will be presented in terms of phonon band diagrams. The phonon density of states $g(\omega)$ is given by

$$g(\omega) = \frac{V}{(2\pi)^3} \int d^3q \sum_{\nu=1}^{3N} \delta(\omega - \omega^\nu(\mathbf{q})), \quad (1)$$

where V denotes the volume of the simulation cell containing N atoms and the mode index ν runs from 1 to the total number of the normal modes $3N$. It is also possible to evaluate the

projected density of phonon modes function for a specified atomic type a using the expression

$$g^a(\omega) \equiv \frac{V}{(2\pi)^3} \int d^3q \sum_a^{3N} (\delta(\omega - \omega_\nu(\mathbf{q}))W_a^\nu(\mathbf{q})). \quad (2)$$

Here $W_a^\nu(\mathbf{q})$, defined in Eq. (11) of Ref. [17], represents the amplitude weight factor of mode ν for atomic type a. By construction, the sum of $g^a(\omega)$ over all atomic types gives the total phonon density of states $g(\omega)$.

From the total phonon density of states, the Helmholtz free energy $F(T)$ in the harmonic approximation for system with fixed volume V and temperature T can be computed according to

$$F(T) = U_{SL} + F_{vib}(T), \quad (3)$$

where $F_{vib}(T)$ is the vibrational contribution to the Helmholtz free energy, or the phonon free energy which takes the following form [25]:

$$F_{vib}(T) = k_B T \int_0^\infty d\omega \, \ln\left[2\sinh\left(\frac{\hbar\omega}{2k_BT}\right)\right]g(\omega). \quad (4)$$

Here k_B is the Boltzmann constant.

Results for the static lattice optimizations, the phonon analyses, and the Helmholtz free-energy analysis for the Li_3BO_3 and Li_3BN_2 structures are given below, focusing first on the monoclinic phases of both materials, known to have measurable ionic conductivity, and then on some of the other phases of Li_3BN_2 that have been identified.

A. Structural analysis of Li_3BO_3

The literature on Li_3BO_3 reports a single crystal phase initially reported by Stewner in 1971 [27] characterized by the monoclinic structure $P2_1/c$ (space group No. 14) [28] with four formula units per conventional unit cell. In preparation for further experimental studies, Li_3BO_3 was prepared at Argonne National Labs by mixing a 3:1 stoichiometric ratio of LiOH monohydrate (Sigma Aldrich) with Boric acid (Sigma Aldrich), respectively. The material was loaded into an alumina crucible, calcined/annealed at 450 °C for 4 h, and finally ground with a mortar and pestle. The powdered samples was then pressed into a pellet (diameter: 0.5″) at 15 MPa, loaded into an alumina crucible, and annealed/sintered at 600 °C for 8 hours. The x-ray diffraction pattern of the resulting powder agreed to high precision with the analysis of Stewner [27].

As shown in Fig. 1, the crystal structure of Li_3BO_3 is constructed from isolated BO_3 units formed into planes with triangular symmetry with the Li ions arranged in the voids of the framework. All contained sites have multiplicity and Wyckoff label 4e. In each unit cell, the Li ions occupy three distinct symmetry positions Li(1), Li(2), and Li(3) as indicated in the structural diagram of Fig. 1 by three different shades of blue. The atomic arrangement makes intuitive sense that the large voids within the structure could facilitate Li ion mobility. Table I summarizes the calculated lattice parameters and fractional coordinates compared with the experimental measurements [27]. The comparison presents a good agreement between computational and experimental results, finding
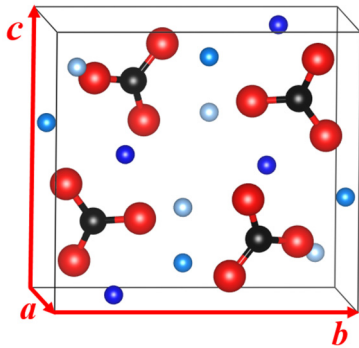
FIG. 1. Ball and stick visualization of Li$_3$BO$_3$ in the monoclinic $P2_1/c$ (No. 14) structure with Li, B, and O represented by blue, black, and red balls, respectively. Three shades of blue are used to indicate the three inequivalent Li sites in this structure.

differences in the lattice parameters of less than 0.05 Å, for example.

To analyze the vibrational modes of Li$_3$BO$_3$, it is efficient to use the primitive unit cell and to use the ABINIT code for evaluating the density-functional perturbation theory, the dynamical matrix, and finding the normal modes. For the primitive cell of Li$_3$BO$_3$, there are 28 atoms per unit cell and 84 vibrational modes which can be decomposed into irreducible representations according to group theory analysis [28]: 21 A_g + 21 A_u + 21 B_g + 21 B_u, comprising three zero-frequency acoustic modes A_u + 2 B_u, infrared active optic modes 20 A_u + 19 B_u, and Raman active optic modes 21 A_g + 21 B_g. The phonon band structure along with the corresponding projected density of states for Li$_3$BO$_3$ are presented in Fig. 2. The low-frequency region less than 650 cm^{-1} involves significant motions of the Li ions while the high phonon modes above 650 cm^{-1} are attributed to primarily BO$_3$ motions with the maximum frequency up to 1379 cm^{-1}. The observed flat modes at around 910 cm^{-1} are characteristic of the internal stretching motion of BO$_3$ units with almost stationary B ions. All real frequencies throughout the vibra-
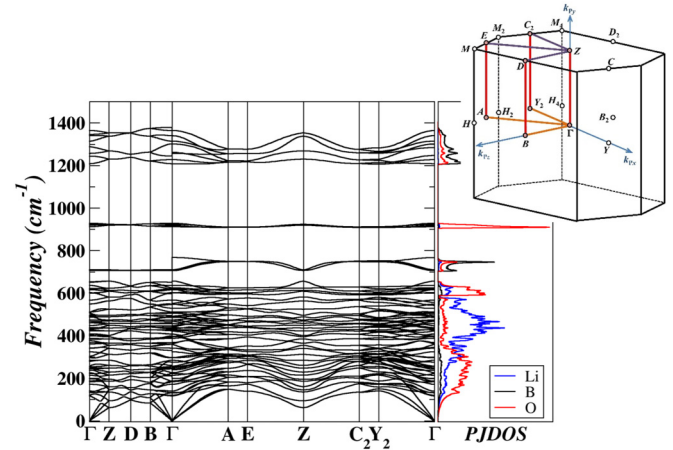

FIG. 2. Phonon dispersion curves and the corresponding projected density states for Li$_3$BO$_3$ in the $P2_1/c$ (No. 14) structure. The Brillouin zone diagram for this structure was reproduced from Hinuma *et al.* in Ref. [29] with permission from the publisher.

tional range suggest that crystalline Li$_3$BO$_3$ is dynamically stable.

B. Structural analysis of Li$_3$BN$_2$

The literature reports at least three crystalline phases for Li$_3$BN$_2$. Yamane *et al.* [30] carefully analyzed the low temperature α and higher temperature β forms, finding the transition temperature to be approximately 1135 K and the melting temperature of the β form to be approximately 1189 K. The high temperature β form could be quenched to room temperature. The α form was initially characterized with the space group $P4_22_12$ (space group No. 94) [28], which was later found to be equivalent to the higher symmetry $P4_2/mnm$ structure [31] (space group No. 136) [28]. The β form was characterized with the monoclinic $P2_1/c$ (space group No. 14) [28]. A distinct tetragonal (γ) phase of Li$_3$BN$_2$ was found by Pinkerton and Herbst [32] with the symmetry $I4_1/amd$ (space group No. 141) [28], obtained by removing hydrogen from fine powders containing LiNH$_2$ and LiBH$_4$. Since the γ phase is synthesized at relative low temperature $T \approx 2500\,^\circ$C, it is not clear how it fits into the overall phase diagram of Li$_3$BN$_2$. Each of

TABLE I. Lattice parameters of Li$_3$BO$_3$ in the $P2_1/c$ (No. 14) structure. The column labeled Wyck lists the conventional cell multiplicity and Wyckoff labels, comparing the present paper (cal) with the experimental analysis of Stewner [27] (exp).

	a (Å)	b (Å)	c (Å)	α (deg)	β (deg)	γ (deg)
Li$_3$BO$_3$ (cal)	3.24	9.16	8.28	90.00	100.98	90.00
Li$_3$BO$_3$ (exp)	3.27	9.18	8.32	90.00	101.05	90.00
			Fractional coordinates (x, y, z)			

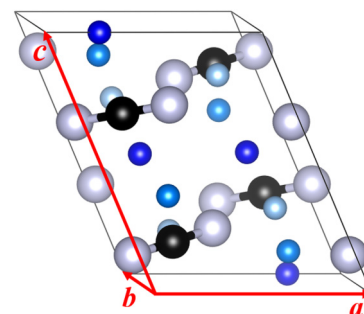| Atom	Wyck	Li$_3$BO$_3$ (cal)	Li$_3$BO$_3$ (exp)
Li(1)	4e	(0.493, 0.233, 0.018)	(0.493, 0.233, 0.018)
Li(2)	4e	(0.276, 0.477, 0.113)	(0.271, 0.477, 0.113)
Li(3)	4e	(−0.091, 0.423, 0.368)	(−0.093, 0.429, 0.367)
B	4e	(0.198, 0.186, 0.255)	(0.198, 0.186, 0.254)
O(1)	4e	(0.028, 0.137, 0.099)	(0.026, 0.139, 0.100)
O(2)	4e	(0.227, 0.093, 0.389)	(0.225, 0.094, 0.386)
O(3)	4e	(0.366, 0.327, 0.279)	(0.361, 0.325, 0.278)

FIG. 3. Ball and stick visualization of a conventional unit cell of β-Li$_3$BN$_2$ having $P2_1/c$ (space group No. 14). Li, B, and N ions are represented by three shades of blue, black, and gray balls, respectively.

TABLE II. Summary of lattice parameters for Li_3BN_2 in the $P2_1/c$ (β form, No. 14), comparing computational (cal) results with experimental measurements (exp).

		a (Å)	b (Å)	c (Å)	α (deg)	β (deg)	γ (deg)
$P2_1/c$ (cal)		5.11	7.00	6.71	90.00	113.08	90.00
$P2_1/c$ (exp [30])		5.15	7.08	6.79	90.00	112.96	90.00
				Fractional coordinates (x, y, z)			
Atom	Wyck	$P2_1/c$ (cal)			$P2_1/c$ (exp [30])		
Li(1)	4e	(0.249, 0.481, 0.498)			(0.250, 0.485, 0.498)		
Li(2)	4e	(0.250, 0.012, 0.375)			(0.252, 0.012, 0.375)		
Li(3)	4e	(0.741, 0.208, 0.314)			(0.744, 0.207, 0.314)		
B	4e	(0.215, 0.320, 0.176)			(0.215, 0.320, 0.176)		
N(1)	4e	(0.437, 0.439, 0.219)			(0.434, 0.437, 0.219)		
N(2)	4e	(0.991, 0.203, 0.135)			(0.994, 0.205, 0.135)		
Ang(N(1)-B-N(2)) (deg)		180.00			180.00		
d(N-B) (Å)		1.342			1.339		

the three characterized phases of Li_3BN_2 is composed of Li ions arranged among linear or nearly linear $(BN_2)^{3-}$ units.

1. Structural analysis of β-Li_3BN_2

While β-Li_3BN_2 has the same space group as Li_3BO_3, its structure looks quite distinct. Figure 3 shows the ball and stick drawing of the ideal β-Li_3BN_2 crystal, which has four formula units in the conventional monoclinic unit cell.

Here we see that the structure is characterized by linear N–B–N units aligned approximately in **ab** planes and spaced along the **c** axis. The Li ions are located in the empty cavities between $(BN_2)^{3-}$ units, with three inequivalent types [Li(1), Li(2), and Li(3)] all having the multiplicity and Wyckoff label 4e. From the viewpoint shown in Fig. 3, it is seen that type Li(3) ions are approximately in the same planes as the $(BN_2)^{3-}$ units, while the Li(1) and Li(2) ions are arranged in different planes along the **c** axis.

The results of the optimized static lattice calculation are reported in Table II. Here we see the comparison with experiments is reasonable with a discrepancy of approximately 0.08 Å or less in the lattice lengths and less than 0.004 in fractional coordinates.

The phonon dispersion curves of β-Li_3BN_2 are presented in Fig. 4. It is interesting to note that the frequencies of several top modes, due to the vibration motions of B–O units, higher by about 400 cm^{-1} than those of Li_3BN_2 in Fig. 2. The diagram also shows nearly flat dispersion curves at around 1100 cm^{-1}, reflecting the typical feature of the internal B–O stretch. Furthermore, all frequencies are found to be positive, indicating that Li_3BN_2 in the β phase is dynamically stable. From these results, we can then estimate the vibrational Helmholtz free energy which will be discussed below.

2. Structural analysis of γ-Li_3BN_2

Figure 5 shows the ball and stick drawing of the ideal γ-Li_3BN_2 crystal which has eight formula units in the conventional tetragonal $I4_1/amd$ unit cell. Here we see that the structure consists of linear N–B–N units aligned along the **a** or **b** axes with Li ions arranged between occupying 16g and 4e sites in the Wyckoff multiplicity and site label convention.

In this structure, it is found that the B–N–B angle is slightly bent in the $I4_1/amd$ structure.

The results of the optimized static lattice calculation are reported in Table III. Here we find a relatively large discrepancy of approximately 0.15 Å in the calculated and measured length of the c lattice parameter while the $a = b$ lattice parameters differ only by 0.04 Å.

The phonon bands calculated from the optimized primitive unit cell of γ-Li_3BN_2 are presented in Fig. 6, with a remarkably similar dispersion profile as seen in Fig. 4 for the β form. Again in this case, we see that all frequencies are found to be positive, indicating that the system is dynamically stable. From these results, we can then estimate the vibrational Helmholtz free energy which will be discussed below.

3. Structural analysis of α-Li_3BN_2 based on literature analysis

Figure 7 shows the ball and stick drawings of α-Li_3BN_2 in the reported $P4_2/mnm$ (No. 136) [31] structure, which has two formula units in the conventional tetragonal unit cell. As illustrated in the figure, the structure is characterized by linear N–B–N units aligned in the **ab** planes with alternating
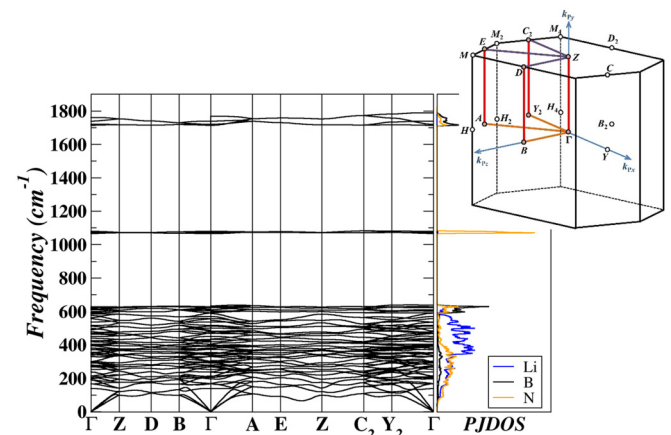

FIG. 4. Phonon dispersion curves and the corresponding projected density states for Li_3BN_2 in the $P2_1/c$ (β form) structure. The Brillouin zone diagram for this structure was reproduced from Hinuma et al. in Ref. [29] with permission from the publisher.

TABLE III. Summary of lattice parameters for Li$_3$BN$_2$ in the $I4_1/amd$ (γ form, No. 141), comparing computational results with experimental measurements.

		a (Å)	b (Å)	c (Å)	α (deg)	β (deg)	γ (deg)
$I4_1/amd$ (cal)		6.56	6.56	10.20	90.00	90.00	90.00
$I4_1/amd$ (exp [32])		6.60	6.60	10.35	90.00	90.00	90.00
				Fractional coordinates (x, y, z)			
Atom	Wyck	$I4_1/amd$ (cal)			$I4_1/amd$ (exp [32])		
Li(1)	8e	(0.000, 0.000, 0.126)			(0.000, 0.000, 0.120)		
Li(2)	16g	(0.275, 0.275, 0.000)			(0.271, 0.271, 0.000)		
B	8e	(0.000, 0.000, 0.354)			(0.000, 0.000, 0.353)		
N	16h	(0.000, 0.205, 0.349)			(0.000, 0.209, 0.345)		
Ang(N-B-N) (deg)		175.61			172.86		
d(N-B) (Å)		1.347			1.382		

directions along the **c** axis and by two crystallographically distinct Li sites as indicated with two shades of blue balls. The Li ion at Wyckoff site d and its four symmetry equivalents are located between the layers of (BN$_2$)$^{3-}$ units while the Li ion at the b site and its two equivalents are located within the (BN$_2$)$^{3-}$ layers. The B atoms are in a bcc arrangement, each is linearly bonded to two N's with straight bond angles. In addition, the orientation of N–B–N bonds in the corners are parallel to each other and are orthogonal to those in the center of the lattice.

The results of the optimized static lattice calculation are reported in Table IV. Here we see the comparison with experiments finds an underestimate of the $a = b$ lattice parameter of 0.01 Å and of the c lattice parameter of 0.11 Å.

The phonon dispersion curves are presented in Fig. 8. Here we see that the phonon mode of the $P4_2/mnm$ structure has imaginary frequencies around M point along M → X, M → Γ, and M → A involving doubly degenerate modes, implying instability of that structure. To check this result, we recalculated the analysis substituting the local density approximation (LDA) [33] for the PBEsol [6] exchange-correlation form. In our experience, the LDA exchange-correlation functional generally models lattice vibrations in closer agreement with the experiment. However, in this case, the same imaginary

modes were found, implying the structure is dynamically unstable and that further analysis is needed to identify the correct structural form of α-Li$_3$BN$_2$.

4. Proposed corrected structure of α-Li$_3$BN$_2$ based on dynamic stability in the harmonic phonon approximation

The analysis of imaginary frequency solutions of the dynamical equations involved with phonon modes has been extensively discussed in the literature [10,34–37]. In the simplest case, the eigenvectors of the imaginary modes indicate lattice distortions associated with lower symmetry phase transitions.

In the present case of the reported $P4_2/mnm$ structure of α-Li$_3$BN$_2$, the results of Fig. 8 suggest that eigenvectors of the two degenerate imaginary modes at the M (0.5, 0.5, 0.0) point in the Brillouin zone should be examined. As illustrated in Fig. 9, which indicates with colored arrows the dominating amplitudes of these two modes, the instability is mainly attributed to the vibrations of b-type Li(2) ions along the **c** axis, perpendicular to the direction of the wave vector **q** at the M point.

Since these modes are associated with the M (0.5, 0.5, 0.0) point of the Brillouin zone of the $P4_2/mnm$ structure, this suggests that the corresponding lattice distortion can best
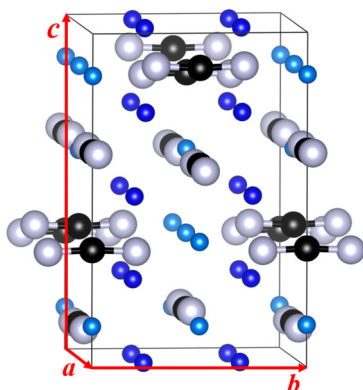

FIG. 5. Ball and stick visualization of a conventional unit cell of γ-Li$_3$BN$_2$ having the $I4_1/amd$ space group No. 141). Li, B, and N ions are represented by two shades of blue, black, and gray balls, respectively.
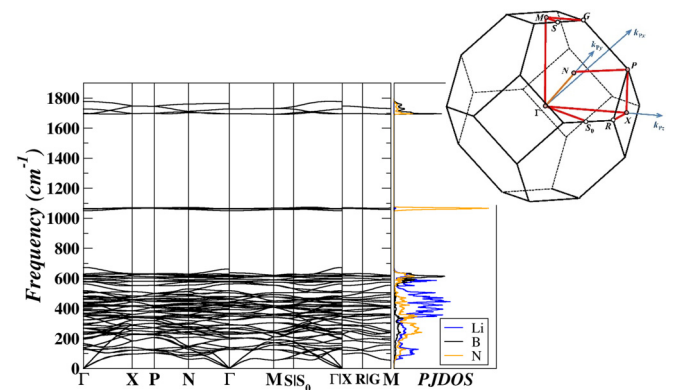

FIG. 6. Phonon dispersion curves and the corresponding projected density states for γ-Li$_3$BN$_2$ in the $I4_1/amd$ structure. The Brillouin zone diagram for this structure was reproduced from Hinuma *et al.* in Ref. [29] with permission from the publisher.

TABLE IV. Summary of lattice parameters for Li_3BN_2 in the $P4_2/mnm$ (α form, No. 136), comparing computational results (cal) with experimental measurements (exp).

		a (Å)	b (Å)	c (Å)	α (deg)	β (deg)	γ (deg)
$P4_2/mnm$ (cal)		4.63	4.63	5.15	90.00	90.00	90.00
$P4_2/mnm$ (exp [31])		4.64	4.64	5.26	90.00	90.00	90.00
				Fractional coordinates (x, y, z)			
Atom	Wyck	$P4_2/mnm$ (cal)			$P4_2/mnm$ (exp [31])		
Li(1)	$4d$	(0.000, 0.500, 0.250)			(0.000, 0.500, 0.250)		
Li(2)	$2b$	(0.000, 0.000, 0.500)			(0.000, 0.000, 0.500)		
B	$2a$	(0.000, 0.000, 0.000)			(0.000, 0.000, 0.000)		
N	$4f$	(0.206, 0.206, 0.000)			(0.204, 0.204, 0.000)		
Ang(N-B-N) (deg)		180.00			180.00		
d(N-B) (Å)		1.346			1.339		

be described in a supercell structure having lattice vectors $(\mathbf{a}_s, \mathbf{b}_s, \mathbf{c}_s)$ along the M directions and related to the conventional $P4_2/mnm$ cell constants (a_c, b_c, c_c) according to

$$\mathbf{a}_s = a_c\hat{\mathbf{x}} + b_c\hat{\mathbf{y}}, \quad \mathbf{b}_s = a_c\hat{\mathbf{x}} - b_c\hat{\mathbf{y}}, \quad \mathbf{c}_s = c_c\hat{\mathbf{z}}. \quad (5)$$

Starting with the $(\mathbf{a}_s, \mathbf{b}_s, \mathbf{c}_s)$ supercell of this structure, we calculated the static lattice parameters using several initial displacements of the b-type Li ions along the $\hat{\mathbf{z}}$ direction and the dominating displacements of the eigenvectors of the imaginary modes shown in Fig. 9. The optimized structure is characterized with the space group symmetry of orthorhombic $Pmmn$ (space group No. 59), a lower energy structure compared to the $P4_2/mnm$ structure based on which this structure for α-Li_3BN_2 was derived. Fig. 10 compares the perfect supercell of the $P4_2/mnm$ structure with the optimized $Pmmn$ structure while Table V lists the detailed comparison of the structural parameters. It is apparent that the visualization of the $Pmmn$ structure is similar to that of the $P4_2/mnm$ structure, except for some small differences in the arrangements of Li ions. The Li sites with Wyckoff labels $4d$ in the supercell of the $P4_2/mnm$ structure have a one-to-one correspondence with those at $8g$ sites in the $Pmmn$ structure with very slight deviations. At the same time, the Li sites with Wyckoff labels $2b$ for the $P4_2/mnm$ structure map to the sites with Wyckoff labels $2a$ and $2b$ in the $Pmmn$ structure, respectively, with small distortion mainly in the **c** direction. Additionally, the
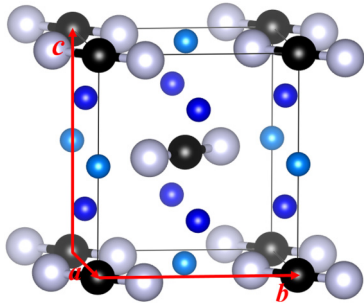
N–B–N bonds of the modified structure experience slight deformation, although the bond lengths remain unchanged, the bond angles are not straight anymore, especially for those in close proximity to the Li ions at the $2a$ sites. From Table V, we see that the distortions relative to the literature structure are very small, so it is understandable that the higher symmetry structure has been reported in previous literature.

To examine the stability of this low-symmetry orthorhombic phase, phonon analysis in the harmonic phonon approximation was performed. Phonon dispersion curves along the main symmetry directions and the projected phonon density of states for $Pmmn$ structure are displayed in Fig. 11. In Table VI, we give the one-to-one mapping relation between the high-symmetry **q** points in the tetragonal $P4_2/mnm$ structure and those in the orthorhombic $Pmmn$ structure. It is notable that the M point which associates with the unstable phonon modes of the $P4_2/mnm$ structure is mapped onto the Γ point, the center of the Brillouin zone, in the $Pmmn$ structure. Unlike the acoustic phonon instabilities exhibited at the M point of the $P4_2/mnm$ structure, from Fig. 11 we see that the $Pmmn$ structure is dynamically stable along various high-symmetry lines throughout the Brillouin zone.

According to group theory (Ref. [28]), the zone-center phonon modes of the α phase in the $Pmmn$ structure are classified into acoustic modes $B_{1u} + B_{2u} + B_{3u}$ and optic modes including infrared active modes $10B_{1u} + 9B_{3u} + 9B_{3u}$ and Raman active modes $11A_g + 5B_{1g} + 10B_{2g} + 10B_{3g}$. The irreducible representation of zone-center phonon modes of the β phase is decomposed of acoustic modes $A_u + 2B_u$, infrared active optic modes $17A_u + 16B_u$, and Raman active optic modes $18A_g + 18B_g$. For the case of γ-Li_3BN_2, the symmetry-adapted phonon modes for Γ point decompose as acoustic modes $A_{2u} + E_u$, infrared active optic modes $5A_{2u} + 9E_u$, and Raman active optic modes $5A_{1g} + 6B_{1g} + 2B_{2g} + 10E_g$. Given this demonstration of the dynamical stability, we propose that the correct structure of α-Li_3BN_2 must be characterized by the $Pmmn$ structure.

C. Comparison of the Helmholtz free energies in the harmonic approximation

From the harmonic phonon results for the stable structures presented in Sec. III, the vibrational contributions to the
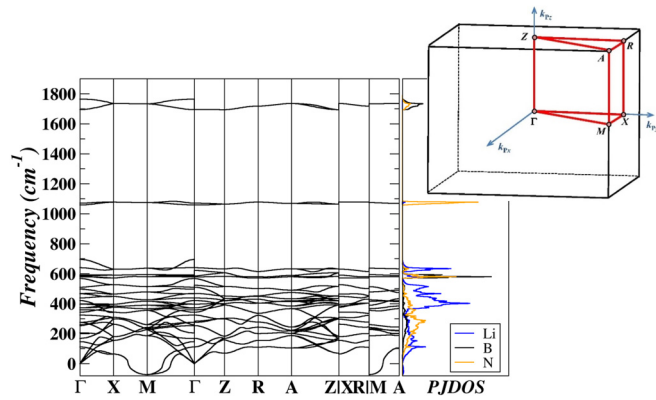

FIG. 7. Ball and stick visualization of a conventional unit cell of α-Li_3BN_2 having the $P4_2/mnm$ (space group No. 136). Li, B, and N ions are represented by two shades of blue, black, and grey balls, respectively.

FIG. 8. Phonon dispersion curves and the corresponding projected density states for Li$_3$BN$_2$ in the $P4_2/mnm$ (α form) structure. The Brillouin zone diagram for this structure was reproduced from Hinuma *et al.* in Ref. [29] with permission from the publisher.

Helmholtz free energy as a function of temperature can be calculated as shown in Fig. 12. This figure shows that, while (understandably) $F_{\mathrm{vib}}(T)$ for Li$_3$BO$_3$ is different from $F_{\mathrm{vib}}(T)$ for Li$_3$BN$_2$, the curves for all three stable phases of Li$_3$BN$_2$ are nearly identical. According to our simulation results, it is interesting to see that the three known structures of Li$_3$BN$_2$, despite their different symmetries and arrangements of component ions, have very similar static lattice U_{SL} energies with a difference in the order of 10^{-3} eV per formula unit, which is close to the expected numerical accuracy of the calculations. Similarly, the phonon densities of states shown in Figs. 4, 6, and 11, while not identical, are also very similar, covering the same range of normal mode frequencies up to about 1800 cm^{-1}. As we can see from these figures, the vibrational amplitudes of the Li ions contribute to mode frequencies less than 600 cm^{-1}, while the vibrations of (BN$_2$)$^{3-}$ ions spread over the whole frequency range. In particular, the pure internal stretching vibrations of (BN$_2$)$^{3-}$ units results in flat dispersion curves with frequencies of about 1100 cm^{-1} in each case. This N-stretching mode is likely to be related to the Raman active spectral feature reported by Somer for α-Li$_3$BN$_2$ at
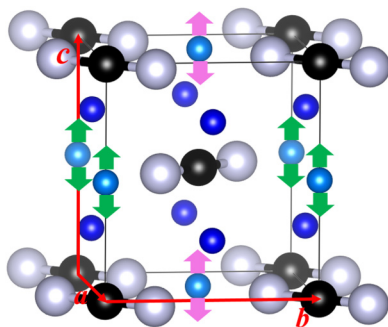

(a)

(b)

FIG. 10. Ball and stick diagrams projected onto the **bc** plane for (a) the supercell of the tetragonal $P4_2/mnm$ structure as defined by Eq. (5) and (b) the optimized orthorhombic $Pmmn$ structure. The ball conventions are the same as for Fig. 7 except that the three crystallographically distinct Li sites of the $Pmmn$ structure are indicated with three shades of blue balls.

1057 cm^{-1} [38]. As a result of these similar phonon distributions, the vibrational contribution to the Helmholtz free energy [Eq. (4)] is nearly identical for the three phases. These results are shown in Fig. 12, which plots $F_{\mathrm{vib}}(T)$ for Li$_3$BO$_3$ and the α, β, and γ phases of Li$_3$BN$_2$. While the phonon free-energy profile for Li$_3$BO$_3$ is distinct from that of Li$_3$BN$_2$, the three phases of Li$_3$BN$_2$ are remarkably similar. This leads to the conclusion that to explain the experimental observation that the α phase is the low temperature phase, a higher level of theory should be considered.

FIG. 9. Ball and stick diagram of the $P4_2/mnm$ structure of Li$_3$BN$_2$, similar to Fig. 7. The up and down arrows indicate the dominating amplitudes of the motions associated with the two eigenvectors of the imaginary phonon modes at the M point of the Brillouin zone involving the Li(2) atoms at b sites. The green and purple arrow colors are used to indicate separate site amplitudes for the group of atoms.
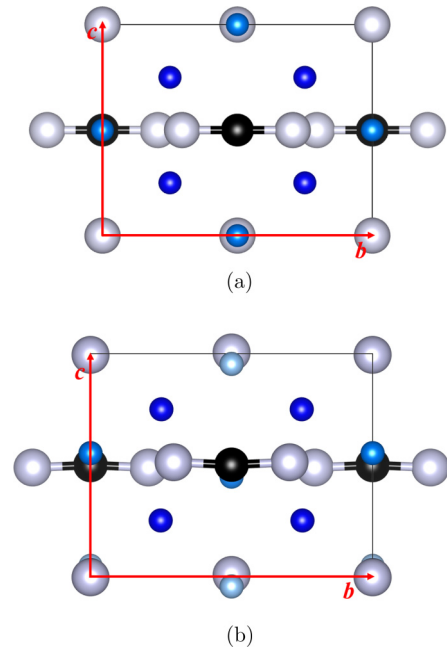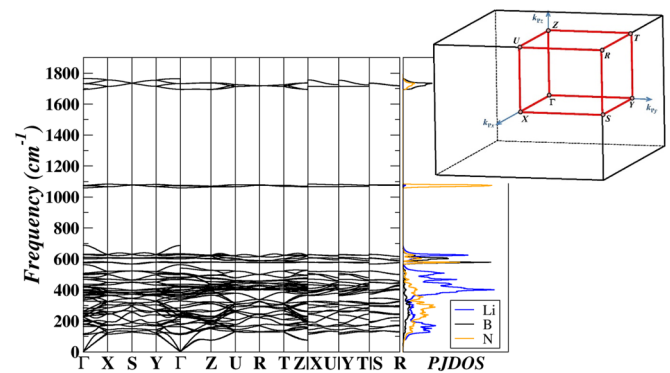

FIG. 11. Phonon dispersion curves along high symmetry directions of the Brillouin zone and the corresponding projected density states for Li$_3$BN$_2$ in the $Pmmn$ structure. The Brillouin zone diagram for this structure was reproduced from Hinuma *et al.* in Ref. [29] with permission from the publisher.

TABLE V. Summary of lattice parameters for the *Pmmn* structure compared to the results on the $P4_2/mnm$ structure in the supercell setting defined in Eq. (5).

		a (Å)	b (Å)	c (Å)	α (deg)	β (deg)	γ (deg)
Pmmn (cal)		6.539	6.543	5.179	90.00	90.00	90.00
Super $P4_2/mnm$ (cal)		6.559	6.559	5.146	90.00	90.00	90.00

		Pmmn			Super $P4_2/mnm$	
Atom	Wyck	(x, y, z)	Atom	Wyck	(x, y, z)
Li(1)	$8g$	(0.239, 0.751, 0.250)	Li(1)	$4d$	(0.250, 0.750, 0.250)
Li(2)	$2a$	(0.000, 0.000, 0.553)	Li(2)	$2b$	(0.000, 0.000, 0.500)
Li(3)	$2b$	(0.500, 0.000, 0.046)	Li(2)	$2b$	(0.500, 0.000, 0.000)
B(1)	$2a$	(0.000, 0.000, 0.004)	B(1)	$2a$	(0.000, 0.000, 0.000)
B(2)	$2b$	(0.500, 0.000, 0.499)	B(1)	$2a$	(0.500, 0.000, 5.000)
N(1)	$4f$	(0.206, 0.000, −0.006)	N(1)	$4f$	(0.205, 0.000, 0.000)
N(2)	$4e$	(0.500, 0.795, 0.488)	N(1)	$4f$	(0.500, 0.795, 0.500)

IV. CORRECTED STRUCTURAL ANALYSIS FOR α-Li$_3$BN$_2$ USING QUASIHARMONIC PHONON ANALYSIS

Having seen some shortcomings of the harmonic phonon analysis discussed in Sec. III, we explored the possibility of a more accurate treatment using the quasiharmonic approximation [10,39,40]. In the harmonic approximation, it is assumed that the optimized static lattice internal energy U_{SL} well approximates the optimal lattice parameters of the system and the vibrational Helmholtz free energy $F_{vib}(T)$ based on second derivatives of U_{SL} with respect to atomic coordinates, evaluated at those lattice parameters, well approximates the phonon contributions to the free energy. However, this approach does not account for temperature-dependent changes in the lattice parameters which may be important for these systems. While this more accurate treatment might be of interest for all the materials of this paper, we focus our attention on α-Li$_3$BN$_2$ in the proposed *Pmmn* structure. For this orthorhombic structure, the lattice angles are all 90° so the temperature dependence is considered for the three lattice lengths a, b, and c. The quasiharmonic generalization of Eq. (3) is given by [40]

$$F^{QH}(T, a, b, c) = U_{SL}(a, b, c) + F_{vib}(T, a, b, c), \quad (6)$$

where the a, b, c arguments here are evaluated on a three-dimensional grid of values. For each a, b, c grid point, the static lattice internal energy $U_{SL}(a, b, c)$ is calculated by self-consistent density-functional optimization of the internal atomic coordinates and its second derivatives with respect to atomic coordinates are evaluated to evaluate the lattice parameter-dependent phonon density of states $g(\omega, a, b, c)$

TABLE VI. The mapping of the high-symmetry **q** points in the $P4_2/mnm$ structure onto the corresponding points in the *Pmmn* structure.

	$P4_2/mnm$	*Pmmn*
A → Z	(0.50, 0.50, 0.50)	(0.00, 0.00, 0.50)
Γ → Γ	(0.00, 0.00, 0.00)	(0.00, 0.00, 0.00)
M → Γ	(0.50, 0.50, 0.00)	(0.00, 0.00, 0.00)
R → R	(0.00, 0.50, 0.50)	(0.50, 0.50, 0.50)
X → S	(0.00, 0.50, 0.00)	(0.50, 0.50, 0.00)
Z → Z	(0.00, 0.00, 0.50)	(0.00, 0.00, 0.50)

according to Eq. (1). Note that for this process to work, it is necessary for the phonon frequencies to be real, for each set of lattice parameters a, b, c as was found to be the case for this *Pmmn* system. We also assume that for the electronically insulating systems considered here, the static lattice energy $U_{SL}(a, b, c)$ is temperature independent. From the phonon densities of states, the vibrational contributions to the Helmholtz free energy $F_{vib}(T, a, b, c)$ can also be determined at each temperature T according to Eq. (4).

In practice, the calculations start with the construction of a three-dimensional $3 \times 3 \times 4$ regular grid of the lattice constants defined in a range of values near the equilibrium values calculated in the harmonic phonon approximation. These are $a_H = 6.5393$ Å, $b_H = 6.5433$ Å, and $c_H = 5.1794$ Å. Consequently, the three-dimensional grid range was chosen to be $6.4599 \leqslant a \leqslant 6.6187$, $6.4639 \leqslant b \leqslant 6.6227$ and $5.1000 \leqslant c \leqslant 5.3381$ in Å units.

For each temperature T, Eq. (6) is directly evaluated at the $3 \times 3 \times 4$ grid points and by using cubic spline interpolation [41], it is now possible to estimate the lattice parameter-dependent Helmholtz free energy $F^{QH}(T, a, b, c)$ as a continuous function of lattice parameters within the original range of evaluated grid points. The physical Helmholtz
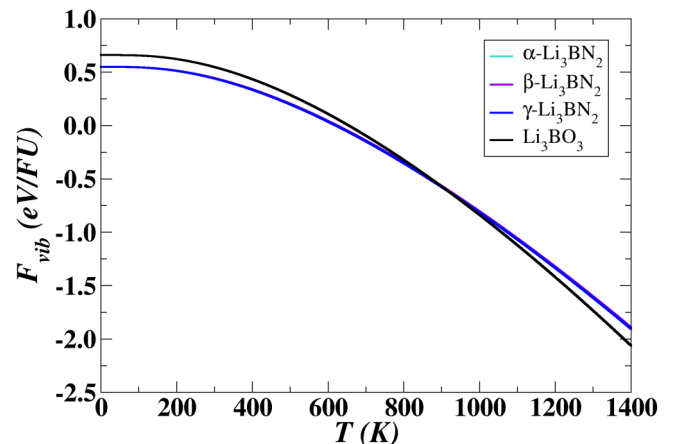

FIG. 12. Plots of $F_{vib}(T)$ [Eq. (4)] for Li$_3$BO$_3$ and Li$_3$BN$_2$ in the α (as corrected in the *Pmmn* structure), β, and γ phases. The curves for the three phases of Li$_3$BN$_2$ are superposed in the figure.
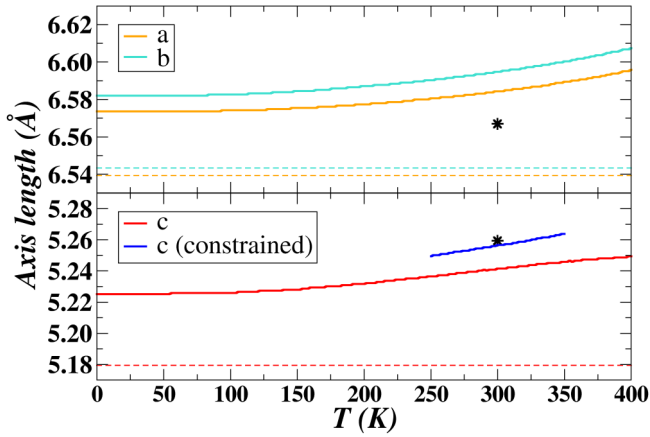
FIG. 13. Lattice parameters a, b, and c in units of Å for α-Li₃BN₂ in the *Pmmn* structure. Full lines represent the temperature-dependent results of the quasiharmonic approximation. The constrained quasiharmonic results are indicated with the full blue line for a range of temperatures near 300 K. Dashed lines represent the temperature-independent results of the harmonic approximation. Experimental results presumed to be measured at room temperature as reported in Ref. [30] and transformed to the *Pmmn* structure are indicated with *.

free energy $[F_{\min}^{\mathrm{QH}}(T)]$ at temperature T is expected to be the minimum value according to

$$F_{\min}^{\mathrm{QH}}(T) = \min_{(a,b,c)} F^{\mathrm{QH}}(T, a, b, c). \qquad (7)$$

The lattice parameters that optimize the right-hand side of Eq. (7) determine the temperature-dependent lattice constants $a(T)$, $b(T)$, and $c(T)$. These are shown in Fig. 13 in comparison with the harmonic phonon values indicated with dashed lines. The quasiharmonic analysis indicates that all three lattice constants generally increase as the temperature increases. The accumulated results are summarized in Table VII. Also included in this table are results which we call constrained quasiharmonic results in which, for temperatures near $T = 300$ K, the a and b lattice parameters are fixed at the experimental values and $F^{\mathrm{QH}}(T, a, b, c)$ is optimized with respect over c.

Examining the quasiharmonic results a little more closely, we noticed that $F^{\mathrm{QH}}(T, a, b, c)$ has an extremely shallow minimum as a function of the lattice parameters, particularly at $T = 300$ K. Figure 14 illustrates contour diagrams of $F^{\mathrm{QH}}(T, a, b, c_{\min})$ and $F^{\mathrm{QH}}(T, a, b_{\min}, c)$ evaluated at $T = 300$ K. Interestingly, these plots show that the depth of the shallow minimum of Helmholtz free energy, which includes
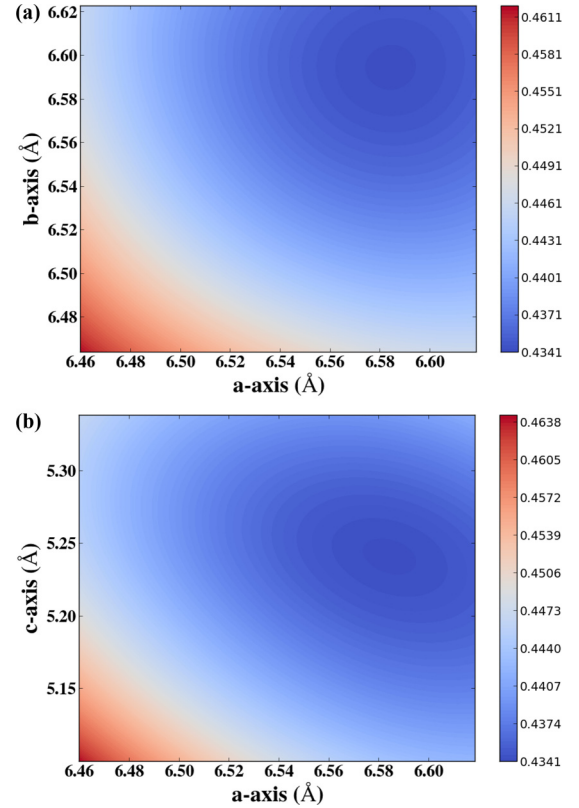

FIG. 14. Contour plots of (a) $F^{\mathrm{QH}}(T = 300\,\mathrm{K}, a, b, c_{\min})$ and (b) $F^{\mathrm{QH}}(T = 300\,\mathrm{K}, a, b_{\min}, c)$ of α-Li₃BN₂ in the *Pmmn* structure. Values of the Helmholtz free energy in units of eV/FU are represented in terms of the color chart shown beside each contour.

the range of the experimental lattice constants, is well within the range of expected errors of the calculation due to physical and numerical approximation of ± 0.001 eV/FU. The numerical values $\Delta F^{\mathrm{QH}}(T = 300\,\mathrm{K}, a, b, c)$ referenced to $F_{\min}^{\mathrm{QH}}(T = 300\,\mathrm{K})$ are listed in the last column of Table VII.

X-ray diffraction patterns from the numerical simulations are shown in Fig. 15, together with the experimental data for the $P4_2/mnm$ structure [31] in the bottom panel. In practice, the experimental curve was generated from the published structural parameters using the same MERCURY software [23] as used to visualize the calculated results. The calculated pattern of the $P4_2/mnm$ structure in the top panel was visually nearly identical to those of the *Pmmn* structure, but slightly incongruent with the experimental observations in the positions of the main peaks. The plots for the *Pmmn* structure using the data obtained from the global and constrained minima of quasiharmonic approximation at $T = 300$ K, however,

TABLE VII. Summary of calculated and experimental lattice parameters (in Å) for α-Li₃BN₃ in the *Pmmn* structure at room temperature (300 K). Last column lists the corresponding value of $F^{\mathrm{QH}}(a, b, c)$ referenced to the optimized value in eV/FU.

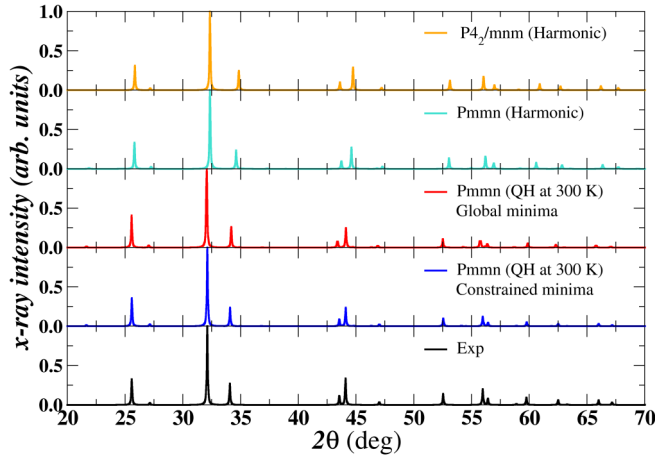|	a	b	c	$\Delta F^{\mathrm{QH}}\,(a, b, c)$
Exp. (Ref. [30])	6.5669	6.5669	5.2593	0.0007
Harmonic phonon approximation	6.5393	6.5433	5.1794	0.0008
QH approximation (unconstrained)	6.5844	6.5947	5.2416	0.0000
QH approximation (constrained))	6.5669	6.5669	5.2566	0.0007

FIG. 15. X-ray diffraction patterns of Li_3BN_2 in the $P4_2/mnm$ and the $Pmmn$ structures approximated in the harmonic phonon approximation (top two panels), in the $Pmmn$ structure approximated in the quasiharmonic approximation at $T = 300$ K (red and blue curves), and experiment of Ref. [30]. The MERCURY software [23] at an x-ray wavelength of $\lambda = 1.54056$ Å was used to generate all the x-ray patterns.

agree very well with the experimental pattern. The results, once again, demonstrate the rationality of the $Pmmn$ structure as a representation for the distorted structure of the $P4_2/mnm$ structure. Furthermore, it shows that the quasiharmonic correction improves the agreement between theory and experiment.

Figure 16 summarizes the Helmholtz free energy as a function of temperature for Li_3BN_2 in the α, β, and γ structures within the harmonic phonon approximation (top plots) together with quasiharmonic approximation results for α-Li_3BN_2. Even in this smaller range, it is apparent that within the harmonic phonon approximation, the Helmholtz free energy of the $Pmmn$ structure is indistinguishable from those of the $P2_1/c$ and $I4_1/amd$ structures throughout the explored temperature range. However, the quasiharmonic plot for the $Pmmn$ structure is below the other three, suggesting a
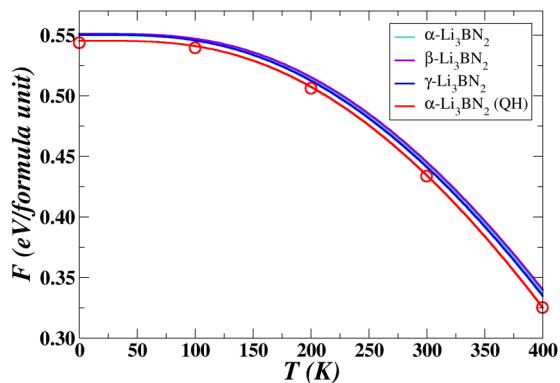

FIG. 16. Plot of Helmholtz free energy in eV/formula unit as a function of T in Kelvin for Li_3BN_2. The results for the $Pmmn$ α (turquoise), β (purple), and the γ (blue) phases are obtained from harmonic approximations, and the quasiharmonic analysis of $F_{min}(T)$ for the $Pmmn$ α phase are displayed in red curve and circles.

relatively stable structure with lower Helmholtz free energy. It is worth mentioning that the red curve representing $F_{min}^{QH}(T)$ is defined by Eq. (7). However, the results shown as red circles for various temperature T are obtained by directly calculating $U_{SL}(a(T), b(T), c(T)) + F_{vib}(T, a(T), b(T), c(T))$ using the lattice parameters $(a(T), b(T), c(T))$ that gives $F_{min}^{QH}(T)$ obtained from the interpolation analysis. The good agreement between the data represented by the curve and the points verifies the accuracy of the interpolation used in these quasiharmonic calculations. Interestingly, because the quasiharmonic optimizes the sum of static lattice energy $U_{SL}(a, b, c)$ and the vibrational free energy $F_{vib}^{QH}(T, a, b, c)$, while the harmonic approximation only optimizes $U_{SL}(a, b, c)$ and calculates $F_{vib}(T)$ at those optimized lattice parameters, the estimated free energies may differ at all temperatures, as seen in Fig. 16. To properly model the phase stability of Li_3BN_2, it would be necessary to perform a more extensive quasiharmonic treatment of the α phase (considering a wider range of lattice parameters) and also consider similar treatments of the β and γ phases. While such compute intensive simulations are certainly manageable, they were considered beyond the scope of the present paper.

V. ANALYSIS OF POSSIBLE CHEMICAL DECOMPOSITION REACTION FOR MONOCLINIC FORMS OF Li_3BO_3 AND β-Li_3BN_2

Since the monoclinic forms of Li_3BO_3 and Li_3BN_2 are of greatest practical interest as electrolyte or coating materials, we focus attention on those phases. To evaluate the chemical stabilities of Li_3BO_3 and β-Li_3BN_2, we estimated the decomposition energy relative to a range of likely products. The stability of a target material or its possible interaction with a second material is estimated from the difference in Helmholtz free energies ΔF of predicted reactions between the reactants **R** and the products **P**. Specifically, the reaction energy is given by

$$\Delta F = \sum_i F_i^P - \sum_j F_j^R. \tag{8}$$

The energy of each material in the reaction is a sum of the static energies of the optimized structures and the phonon contributions according to the harmonic phonon approximation [Eq. (3)]. We used this approach to study both decomposition of the materials themselves, and also their reactivity with Li meta.

The results for decomposition are summarized in Table VIII. For each predicted decomposition reaction, the energy difference ΔF, calculated according to Eq. (8), includes contributions from both the static lattice energy and the phonon free energy of each material. Since the temperature-dependent electronic excitation of metallic Li is trivial, the contribution was not counted. It is worth mentioning for both materials, the energy from vibrational contribution is quite small compared to the static lattice part, indicating that the static lattice energy plays a dominant role in determining the stabilities. The positive ΔF of these proposed pathways suggests endothermic reactions, meaning the left-side reactants need to absorb energy to achieve the decomposition. While this is not an exhaustive study, it does provide some

TABLE VIII. Computed energy differences for reactions indicated by the first column. All energies are given in eV units and the phonon vibrational energy F_{vib} is evaluated at T = 300 K.

Crystal	Reaction: $R \rightarrow P$	ΔU_{SL}	ΔF_{vib}	ΔF
Li$_3$BO$_3$	Li$_3$BO$_3 \rightarrow$ LiBO$_2$[a]+Li$_2$O[b]	0.55	0.06	0.61
	Li$_3$BO$_3 \rightarrow \frac{3}{2}Li_2$O $+ \frac{1}{2}$B$_2$O$_3$[c]	1.40	0.07	1.47
	Li$_3$BO$_3 \rightarrow \frac{1}{3}LiB_3O_5$[d]$+ \frac{4}{3}Li_2$O	1.12	0.04	1.16
β-Li$_3$BN$_2$	β-Li$_3$BN$_2 \rightarrow$ Li$_3$N[e]+BN[f]	0.85	0.09	0.94
	β-Li$_3$BN$_2 \rightarrow \frac{7}{3}$Li[g] $+ $B[h] $+ \frac{2}{3}$LiN$_3$[i]	4.69	−0.07	4.62

[a]Tetragonal (γ-LiBO$_2$) with Space Group $I-42d$ (No. 122); from Ref. [42].
[b]Cubic with Space Group $Fm\bar{3}m$ (No. 225); from Ref. [43].
[c]Orthorhombic with Space Group $Cmc2_1$ (No. 36); from Ref. [44].
[d]Orthorhombic with Space Group $Pna2_1$ (No. 33); from Ref. [45].
[e]Hexagonal with Space Group $P6/mmm$ (No. 191); from Ref. [46].
[f]Cubic with Space Group $Fm\bar{3}m$ (No. 225).
[g]Cubic with Space Group $Im\bar{3}m$ (No. 229).
[h]Rhombohedral with Space Group $R\bar{3}m$ (No. 166); from Ref. [47].
[i]Monoclinic with Space Group $C2/m$ (No. 12); from Ref. [48].

confidence for stating that the Li$_3$BO$_3$ and β-Li$_3$BN$_2$ are chemically stable at room temperature.

In anticipation of the use of Li$_3$BO$_3$ and β-Li$_3$BN$_2$ as coating materials or electrolytes in batteries with metallic Li anodes, we also examined some possible reactions between the electrolyte materials and metallic Li as the results summarized in Table IX. The positive reaction energy ΔF, calculated using Eq. (8) for each predicted reaction, indicates that the interactions with metallic Li are stable at equilibrium at 300 K.

VI. MODELS OF IDEALIZED INTERFACES OF MONOCLINIC FORMS OF Li$_3$BO$_3$ AND β-Li$_3$BN$_2$ WITH LAYERS OF LI ANODE MATERIAL

A. Interface configurations and energetics

To model the possible use of Li$_3$BO$_3$ and β-Li$_3$BN$_2$ for battery applications with pure Li metal anodes, we performed some simulations of model interfaces, using an approach similar to that of Lepley and Holzwarth [49] and references cited therein.

Modeling interfaces between the electrolyte and electrode starts with identifying the plausible cleavage plane for constructing a surface. For a supercell in a slab geometry including vacuum, it is convenient to evaluate the extra energy needed for surface formation according to

$$\gamma_s = \frac{E_{\text{slab}} - nE_{\text{bulk}}}{2A_s}. \qquad (9)$$

TABLE X. Surface energies for several likely surface cleavage planes of Li$_3$BO$_3$ (LBO) and β-Li$_3$BN$_2$ (LBN) electrolytes [γ_s in units of (eV/Å^2)].

Plane	γ_s(LBO)	γ_s(LBN)
[100]	0.048	0.243
[010]	0.057	0.076
[001]	0.051	0.042

Here E_{slab} denotes the total energy of the slab configuration containing n formula units of the bulk electrolyte exposed in a vacuum region. E_{bulk} denotes the total energy per formula unit of the bulk electrolyte. $2A_s$ accounts for two surface plane areas in the periodic simulation cell. Generally, E_{slab} achieves convergence when the length of vacuum norm to the surface is comparable to the lattice constant of the bulk material in the same direction.

The interface properties between two materials can be quantitively measured using the interface energy. For an interface slab made up from the electrolyte material a and the electrode material b, the interface energy γ_{ab} is defined by the equation [49]

$$\gamma_{ab}(\Omega, n_b) = \frac{E(\Omega, A_i, n_a, n_b) - n_a E_a - n_b E_b}{2A_i}, \qquad (10)$$

where A_i represents the interface contact area, n_a and n_b denote the number of formula units of materials a and b, whose bulk energies per formula unit are E_a and E_b, respectively. $E(\Omega, A, n_a, n_b)$ is the total electronic energy of the optimized interface configuration Ω. The calculations of $\gamma_{ab}(\Omega)$ with respect to the number of metallic Li ions, in turn, result in a linear equation of the form

$$\gamma_{ab}(\Omega, n_b) = \gamma_{ab}^{\lim}(\Omega) - \sigma_i n_b. \qquad (11)$$

Here the slope of the best-fitting line σ_i denotes the interface strain factor which characterizes the strain energy associated with holding the electrolyte and electrode materials together. The intercept value of $\gamma_{ab}^{\lim}(\Omega)$ can be used to reference the energy of a coherent interface formed by two perfect compatibility lattice planes with zero strain.

For understanding the interface properties, we simulated the idealized interfaces between the electrolytes in contact with pure lithium metal, Li$_3$BO$_3$/Li and β-Li$_3$BN$_2$/Li, using a periodic arrangement of electrolytes and metallic slabs.

Using Eq. (9), the surface energies for several selected cleavage planes of the Li$_3$BO$_3$ and β-Li$_3$BN$_2$ were calculated as the results listed in Table X. For Li$_3$BO$_3$, the [100] and [001] vacuum cleavages were found to have relatively lower

TABLE IX. Some predicted reactions for interfaces Li$_3$BO$_3$/Li and Li$_3$BN$_2$/Li. The Li metal is assumed to have the optimized bcc [space group $Im\bar{3}m$ (No. 229)] structure.

Crystal	Reaction: $R \rightarrow P$	ΔU_{SL}	ΔF_{vib}	ΔF
Li$_3$BO$_3$	Li$_3$BO$_3 + \frac{3}{4}$Li $\rightarrow \frac{3}{4}$LiBO$_2 + \frac{1}{4}$B $+ \frac{3}{2}$Li$_2$O	0.19	0.07	0.26
	Li$_3$BO$_3 +$ Li $\rightarrow 2$Li$_2$O $+ \frac{1}{3}$B $+ \frac{1}{3}$B$_2$O$_3$	0.64	0.08	0.72
β-Li$_3$BN$_2$	β-Li$_3$BN$_2 + 3$Li $\rightarrow 2$Li$_3$N+B	1.91	0.06	1.97
	β-Li$_3$BN$_2 + \frac{3}{2}$Li $\rightarrow \frac{3}{2}$Li$_3$N $+ \frac{1}{2}$B $+ \frac{1}{2}$BN	1.38	0.07	1.45

(a)

(b)

(c)
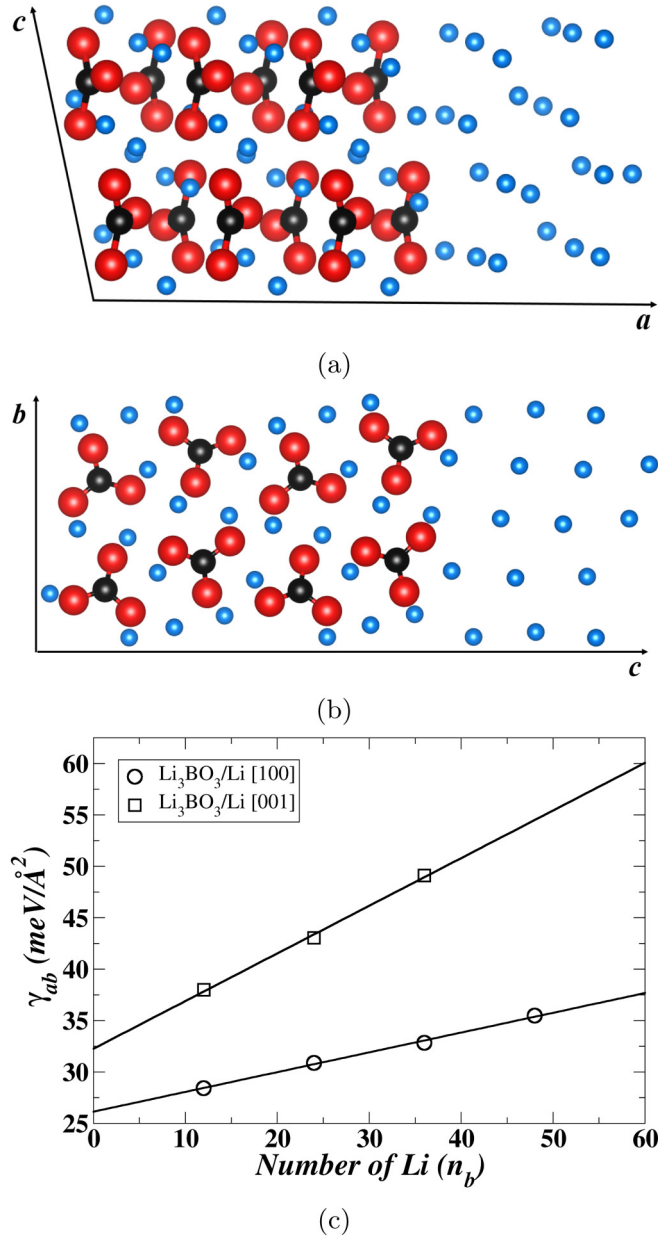
FIG. 17. Ball and stick diagrams of optimized interface structures between (a) $3 \times 1 \times 1$ supercell of Li_3BO_3 and Li slab in [100] direction, viewed in a projection onto the **ac** plane, and (b) $2 \times 1 \times 2$ supercell of Li_3BO_3 and Li slab in [001] direction viewed in a projection onto the **bc** plane. Both configurations contain 24 Li ions in the electrode. The Li, B, and O sites are represented with blue, black, and red balls, respectively. (c) Plot of interface energy γ_{ab} as a function of the number of Li ions in Li metal.

surface energy while, for β-Li_3BN_2, it shows that the energetically most favorable surface is the [001] cleavage with surface energy of $0.042 \, eV/Å^2$.

As illustrated in Fig. 17, two possible ideal models of the interface between the electrolyte Li_3BO_3 and the Li anode material are investigated. The corresponding example configurations are constructed from the optimized structure of multiple pure metallic Li layers placed on the [100] and [001] surfaces of a Li_3BO_3 slab, respectively. In both cases, the Li
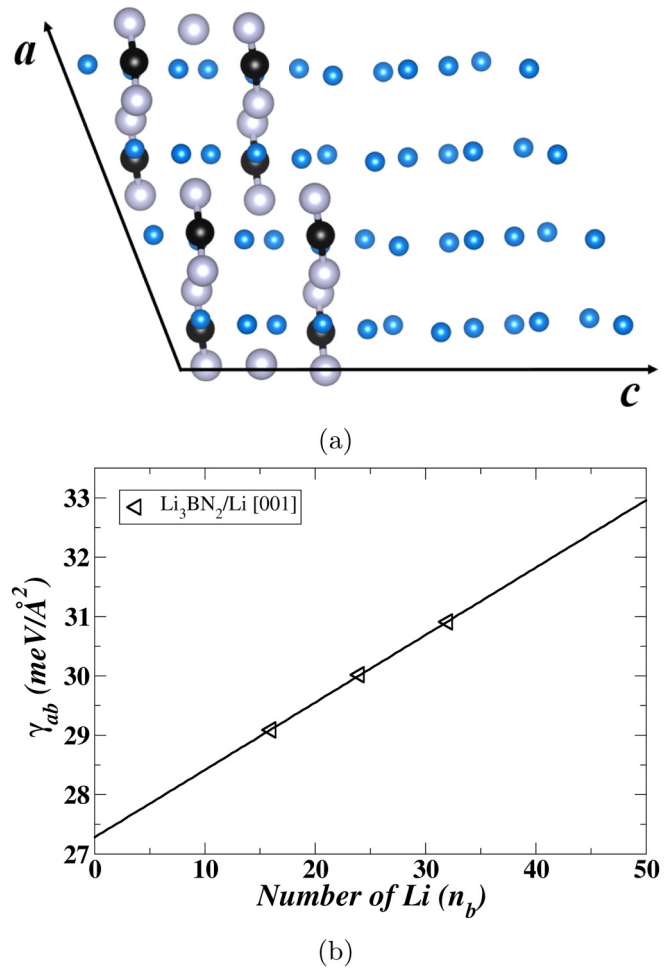

(a)

(b)

FIG. 18. (a) Ball and stick diagrams of optimized interface structures between $2 \times 1 \times 1$ supercell of β-Li_3BN_2 and 24 metallic Li ions in [001] direction, viewed in a projection of the **ac** plane. The Li, B, and N sites are represented with blue, black, and gray balls, respectively. (b) Plot of interface energy γ_{ab} as a function of the number of Li ions in Li metal.

atoms in the metal, retaining a comparable density of fcc Li, are relaxed to a pattern dissimilar to any phase of bulk Li.

Figure 18(a) shows one ideal β-Li_3BN_2/Li interface configuration in the [001] direction. The metallic Li ions, initially in fcc crystalline layout, relaxed to a pattern resembling that of Li ions in the bulk β-Li_3BN_2, presenting remarkable continuity across the interface plane. In addition, the clear-cut distinction between β-Li_3BN_2 and Li metal indicates the stability of the possible interface structure.

The interface energies are analyzed based on the model with a fixed number of atoms in the electrolyte and varying numbers of Li atoms contained in metallic slabs. In practice, only the lattice constant in the direction perpendicular to the interface of the trial structures is allowed to change. By carrying out such constrained calculations, the optimized lattice constants and the minimum energy of the simulation slab are determined. Figures 17(c) and 18(b) display the optimized total energy of the supercell as a function of the number of metallic Li atoms for Li_3BO_3 and β-Li_3BN_2, respectively, with the results listed in Table XI. In the case of Li_3BO_3, the

TABLE XI. Summary of the calculated values of $\gamma_{ab}^{\mathrm{lim}}$ in units of meV/Å^2 and the strain energies σ_i in units of meV/Å^2/Li for interface configurations indicated by the first column.

Configuration	$\gamma_{ab}^{\mathrm{lim}}$	σ_i	Visualization
LBO[100]/Li	26.13	19.00	Fig. 17(a)
LBO[001]/Li	32.26	46.33	Fig. 17(b)
LBN[001]/Li	27.28	0.11	Fig. 18(a)

extrapolated interface energy of the electrolyte $\gamma_{ab}^{\mathrm{lim}}$ for the interface normal to [100] is 26.13 meV/Å^2, and the strain factor σ_i of the metallic Li in particular configuration, obtained from the slope of the linear fitting line, is 19.00 meV/Å^2/Li while for the interface normal to [001], the extrapolated interface energy is $\gamma_{ab}^{\mathrm{lim}} = 32.26$ meV/Å^2 and the strain factor σ_i is up to 46.33 meV/Å^2/Li. It seems that the interface configuration along the a axis is more viable. In the case of β-Li$_3$BN$_2$, the interface energy $\gamma_{ab}^{\mathrm{lim}} = 27.28$ meV/Å^2 at the [001] orientation is comparable to those of Li$_3$BO$_3$, however, the lattice strain factor at the interface is as low as 0.11 meV/Å^2/Li, suggesting it is relatively easy to bring the two material systems into alignment.

B. Electronic density of states analysis

To gain insight into the electronic structures of the plausible Li$_3$BO$_3$/Li and β-Li$_3$BO$_3$/Li interfaces, it is helpful to analyze the partial densities of states $N^a(E)$ which we evaluated according to Eq. (2) in Ref. [50]. $N^a(E)$ evaluates the weighted electronic density of states using a weight factor defined by the charge within the augmentation sphere surrounding the specified atomic type and averaged for all spheres of that type. In this paper, the augmentation radii are $r_c^{\mathrm{Li}} = 1.6$, $r_c^{\mathrm{B}} = 1.4$, $r_c^{\mathrm{O}} = 1.2$, and $r_c^{\mathrm{N}} = 1.2$ in units of Bohr. The results are shown in Figs. 19(a) and 19(b), each with separate $N^a(E)$ contributions for the three forms of Li, the interface, and the interior of electrolyte regions.

The Fermi level, due to the placement of the metallic Li layers, is found to be below the unoccupied conduction bands of the electrolytes with values of 3.64 eV and 2.71 eV for Li$_3$BO$_3$/Li and β-Li$_3$BN$_2$/Li, respectively. It is observed that for each material, the interface and bulk electrolyte have quite similar partial density of states profiles, suggesting the states are relatively consistent during the transition from the bulk electrolyte to the interface geometry in contact with Li metal.

VII. SUMMARY AND CONCLUSIONS

In summary, we have studied the structural and interface properties for the crystal structures of Li$_3$BO$_3$ and Li$_3$BN$_2$ using first-principles simulation techniques. Li$_3$BO$_3$ and Li$_3$BN$_2$ were comparatively investigated in this paper for the reason that they have some structural similarities and also in preparation for their expected future development for battery technology. While Li$_3$BO$_3$ crystallizes in the monoclinic $P2_1/c$ structures, Li$_3$BN$_2$ has three reported structures $P4_2/mnm$ (α form), $P21/c$ (β form), and $I4_1/amd$ (γ form), respectively, in the experiment. Generally, our structural optimizations are in good agreement with the experimental
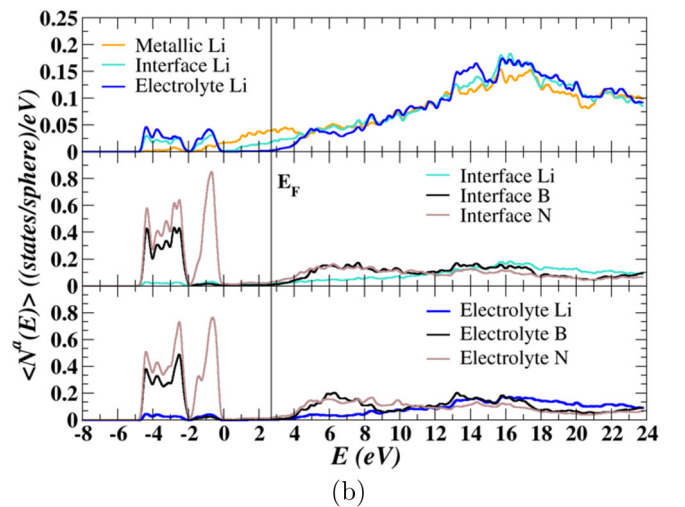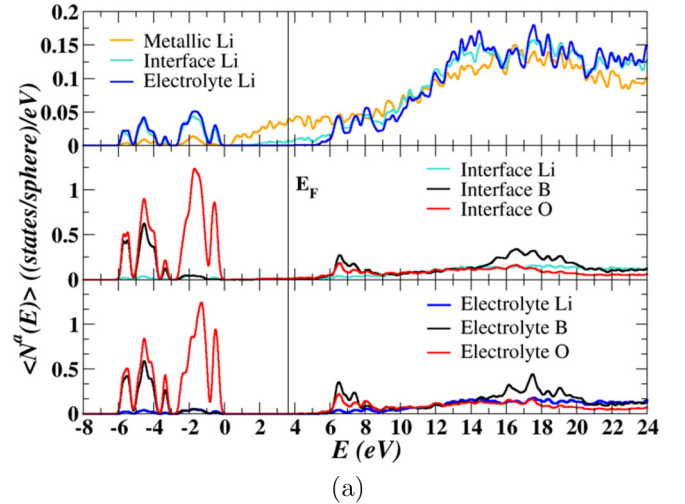

(a)

(b)

FIG. 19. Plots of partial densities of states, in units of states (approximate charge) within the augmentation sphere per eV, for (a) Li$_3$BO$_3$ corresponding to configuration shown in Figs. 17(a) and (b) β-Li$_3$BN$_2$ corresponding to configuration shown in Fig. 18(a). The zero of energy for each subplot was adjusted to the top of the filled valence band.

measurement. However, the phonon analysis shows that the reported α phase of Li$_3$BN$_2$ in the tetragonal symmetry is dynamically unstable due to the imaginary phonon modes at M point. The correct α phase is found to have the *Pmmn* orthorhombic structure containing twice formula units as many as the tetragonal unit cell. The excellent agreement between the x-ray diffraction results of the quasiharmonic approximation on the orthorhombic structure and the experimental pattern provide further evidence of the *Pmmn* structure of α-Li$_3$BN$_2$.

Results find the calculated structures of Li$_3$BO$_3$ and β-Li$_3$BN$_2$ to be stable with respect to the possible decomposition reactions summarized in Table VIII. Since the three crystalline forms of Li$_3$BN$_2$ are equivalently favorable in terms of harmonic Helmholtz free energy, it is expected that the stability results on β-Li$_3$BN$_2$ are also tenable for the γ and α phases of Li$_3$BN$_2$. In addition, we have evaluated the

phase stability of the possible interface geometries between the metallic Li anode and the relatively high ionic conducting electrolytes: Li_3BO_3 and β-Li_3BN_2. On one hand, the quantitative results suggest that both Li_3BO_3/Li and β-Li_3BN_2/Li interfaces are thermodynamically stable considering the endothermic reactions as listed in Table IX. On the other hand, the direct modeling of the supercell in the presence of metallic Li ions allows us to visualize the physical and chemical stabilities of the interfaces in Figs. 17 and 18(a). For Li_3BO_3/Li, the interface configuration along [100] is more probable than that along [001] because of the smaller γ_{ab}^{lim} associated with the effects of lattice strain. For β-Li_3BN_2/Li, the trivial γ_{ab}^{lim} of the (001) plane indicates a more likely realized interface for this system.

The simulated results for the Li_3BO_3/Li and β-Li_3BN_2/Li interfaces found in Sec. VI and the estimated chemical stability of Li_3BO_3 and β-Li_3BN_2 with Li metal summarized in Table IX encourage the development of these electrolytes as interfaces with Li anodes. The results are somewhat reminiscent of earlier studies on LiPON related materials [49,51] which provided insight into the demonstrated viability [52] of this pioneering solid electrolyte for developing all solid-state batteries. In fact, several simulations [49,51,53] suggest that LiPON is chemically reactive with Li metal, tending to form Li_2O, Li_3P, and $LiPN_2$. A recent *in situ* electron microscopic study of a LiPON/Li interface showed [54] that an effective passivating layer tends to form in this system, providing the observed stability with Li anodes. The results of Table IX showing that Li_3BO_3 and β-Li_3BN_2 are unreactive with Li suggest that these boron materials may form stable interfaces with Li anodes without the need for a passivating layer.

[1] Y. Li, Z. D. Hood, and N. A. W. Holzwarth, Phys. Rev. Materials **5**, 085402 (2021).

[2] P. Hohenberg and W. Kohn, Phys. Rev. **136**, B864 (1964).

[3] W. Kohn and L. J. Sham, Phys. Rev. **140**, A1133 (1965).

[4] P. E. Blöchl, Phys. Rev. B **50**, 17953 (1994).

[5] N. A. W. Holzwarth, A. R. Tackett, and G. E. Matthews, Comput. Phys. Commun. **135**, 329 (2001), http://pwpaw.wfu.edu.

[6] J. P. Perdew, A. Ruzsinszky, G. I. Csonka, O. A. Vydrov, G. E. Scuseria, L. A. Constantin, X. Zhou, and K. Burke, Phys. Rev. Lett. **100**, 136406 (2008).

[7] P. Giannozzi, S. de Gironcoli, P. Pavone, and S. Baroni, Phys. Rev. B **43**, 7231 (1991).

[8] X. Gonze, Phys. Rev. B **55**, 10337 (1997).

[9] X. Gonze and C. Lee, Phys. Rev. B **55**, 10355 (1997).

[10] S. Baroni, S. De Gironcoli, A. Dal Corso, and P. Giannozzi, Rev. Mod. Phys. **73**, 515 (2001).

[11] P. Giannozzi and S. Baroni, in *Handbook of Materials Modeling*, edited by S. Yip (Springer, The Netherlands, 2005), pp. 195–214.

[12] X. Gonze, F. Jollet, F. A. Araujo, D. Adams, B. Amadon, T. Applencourt, C. Audouze, J.-M. Beuken, J. Bieder, A. Bokhanchuk, E. Bousquet, F. Bruneval, D. Caliste, M. Côté, F. Dahm, F. D. Pieve, M. Delaveau, M. D. Gennaro, B. Dorado, C. Espejo *et al.*, Comput. Phys. Commun. **205**, 106 (2016), https://www.abinit.org.

[13] X. Gonze, B. Amadon, G. Antonius, F. Arnardi, L. Baguet, J.-M. Beuken, J. Bieder, F. Bottin, J. Bouchet, E. Bousquet *et al.*, Comput. Phys. Commun. **248**, 107042 (2020), https://www.abinit.org/.

[14] P. Giannozzi, O. Andreussi, T. Brumme, O. Bunau, M. Buongiorno Nardelli, M. Calandra, R. Car, C. Cavazzoni, D. Ceresoli, M. Cococcioni *et al.*, J. Phys.: Condens. Matter **29**, 465901 (2017)

[15] P. Giannozzi, O. Baseggio, P. Bonfà, D. Brunato, R. Car, I. Carnimeo, C. Cavazzoni, S. de Gironcoli, P. Delugas, F. Ferrari Ruffino, A. Ferretti, N. Marzari, I. Timrov, A. Urru, and S. Baroni, J. Chem. Phys. **152**, 154105 (2020), http://quantumespresso.org.

[16] H. J. Monkhorst and J. D. Pack, Phys. Rev. B **13**, 5188 (1976).

[17] Y. Li, Z. D. Hood, and N. A. W. Holzwarth, Phys. Rev. Mater. **4**, 045406 (2020).

[18] MATLAB, 2021, *version 9.10.0.1602886 (R2021a)* (The MathWorks Inc., Natick, MA, 2010).

[19] https://www.python.org.

[20] K. Momma and F. Izumi, Appl. Crystallogr. **44**, 1272 (2011), code available from http://jp-minerals.org/vesta/en/.

[21] A. Kokalj, Comput. Mater. Sci. **28**, 155 (2003), code available at http://www.xcrysden.org.

[22] H. T. Stokes and D. M. Hatch, J. Appl. Crystallogr. **38**, 237 (2008), http://iso.byu.edu/iso/isotropy.php.

[23] C. F. Macrae, I. Sovago, S. J. Cottrell, P. T. A. Galek, P. McCabe, E. Pidcock, M. Platings, G. P. Shields, J. S. Stevens, M. Towler, and P. A. Wood, J. Appl. Crystallogr. **53**, 226 (2020).

[24] M. Born and K. Huang, *Dynamical Theory of Crystal Lattices* (Oxford University Press, Oxford, England, 1954).

[25] A. A. Maradudin, E. W. Montroll, G. H. Weiss, and I. P. Ipatova, *Theory of Lattice Dynamics in the Harmonic Approximation*, 2nd ed., Solid State Physics: Supplement, Vol. 3 (Academic Press, Cambridge, MA, 1971).

[26] X. Gonze, Phys. Rev. A **52**, 1086 (1995).

[27] V. F. Stewner, Acta Crystallogr. Sect. B **27**, 904 (1971).

[28] M. I. Aroyo, J. M. Perez-Mato, D. Orobengoa, E. Tasci, G. De La Flor, and A. Kirov, Bulgarian Chem. Commun. **43**, 183 (2011), http://www.cryst.ehu.es/.

[29] Y. Hinuma, G. Pizzi, Y. Kumagai, F. Oba, and I. Tanaka, Comput. Mater. Sci. **128**, 140 (2017).

[30] H. Yamane, S. Kikkawa, and M. Koizumi, J. Solid State Chem. **71**, 1 (1987).

[31] K. Cenzual, L. M. Gelato, M. Penzo, and E. Parthé, Acta Crystallogr. Sect. B **47**, 433 (1991).

[32] F. E. Pinkerton and J. F. Herbst, J. Appl. Phys. **99**, 113523 (2006).

[33] J. P. Perdew and Y. Wang, Phys. Rev. B **45**, 13244 (1992).

[34] L. L. Boyer and J. R. Hardy, Phys. Rev. B **24**, 2577 (1981).

[35] A. I. M. Rae, J. Phys. C **15**, 1883 (1982).

[36] J. D. Althoff, P. B. Allen, R. M. Wentzcovitch, and J. A. Moriarty, Phys. Rev. B **48**, 13253 (1993).

[37] M. Buongiorno Nardelli, S. Baroni, and P. Giannozzi, Phys. Rev. B **51**, 8060 (1995).

[38] M. Somer, Z. Naturforsch. **46b**, 1664 (1991).

[39] S. Baroni, P. Giannozzi, and E. Isaev, Rev. Mineral. Geochem. **71**, 39 (2010).

[40] J. Howard, Z. D. Hood, and N. A. W. Holzwarth, Phys. Rev. Mater. **1**, 075406 (2017).

[41] C. de Boor, *A Practical Guide to Splines* (Springer, New York, NY, 2001).

[42] M. Marezio and J. P. Remeika, J. Chem. Phys. **44**, 3348 (1966).

[43] T. W. D. Farley, W. Hayes, S. Hull, M. T. Hutchings, and M. Vrtis, J. Phys.: Condens. Matter **3**, 4761 (1991).

[44] C. T. Prewitt and R. D. Shannon, Acta Crystallogr. Sect. B **24**, 869 (1968).

[45] H. König and R. Hoppe, Z. Anorg. Allg. Chem. **439**, 71 (1978).

[46] A. Huq, J. W. Richardson, E. R. Maxey, D. Chandra, and W.-M. Chien, J. Alloys Compd. **436**, 256 (2007).

[47] B. Morosin, A. W. Mullendore, D. Emin, and G. A. Slack, AIP Conf. Proc. **140**, 70 (1986).

[48] G. E. Pringle and D. E. Noakes, Acta Crystallogr. Sect. B **24**, 262 (1968).

[49] N. D. Lepley and N. A. W. Holzwarth, Phys. Rev. B **92**, 214201 (2015).

[50] L. E. Rush, Z. D. Hood, and N. A. W. Holzwarth, Phys. Rev. Mater. **1**, 075405 (2017).

[51] N. D. Lepley, N. A. W. Holzwarth, and Y. A. Du, Phys. Rev. B **88**, 104103 (2013).

[52] J. Li, C. Ma, M. Chi, C. Liang, and N. J. Dudney, Adv. Energy Mater. **5**, 1401408 (2015).

[53] Y. Zhu, X. He, and Y. Mo, ACS Appl. Mater. Interfaces **7**, 23685 (2015).

[54] Z. D. Hood, X. Chen, R. L. Sacci, X. Liu, G. M. Veith, Y. Mo, J. Niu, N. J. Dudney, and M. Chi, Nano Lett. **21**, 151 (2021).